Geometric Unmixing of Large Hyperspectral Images: A Barycentric Coordinate Approach

Paul Honeine, *Member, IEEE*, and Cédric Richard, *Senior Member, IEEE*

Abstract—In hyperspectral imaging, spectral unmixing is one of the most challenging and fundamental problems. It consists of breaking down the spectrum of a mixed pixel into a set of pure spectra, called endmembers, and their contributions, called abundances. Many endmember extraction techniques have been proposed in literature, based on either a statistical or a geometrical formulation. However, most, if not all, of these techniques for estimating abundances use a least-squares solution. In this paper, we show that abundances can be estimated using a geometric formulation. To this end, we express abundances with the barycentric coordinates in the simplex defined by endmembers. We propose to write them in terms of a ratio of volumes or a ratio of distances, which are quantities that are often computed to identify endmembers. This property allows us to easily incorporate abundance estimation within conventional endmember extraction techniques, without incurring additional computational complexity. We use this key property with various endmember extraction techniques, such as N-Findr, vertex component analysis, simplex growing algorithm, and iterated constrained endmembers. The relevance of the method is illustrated with experimental results on real hyperspectral images.

Index Terms—Abundance estimation, Cramer's rule, endmember extraction, hyperspectral image, iterated constrained endmembers algorithm, N-Findr, orthogonal subspace projection, simplex, simplex growing algorithm, unmixing spectral data, vertex component analysis.

I. INTRODUCTION

THE EMERGENCE of hyperspectral imaging sensors in recent years has brought new opportunities and challenges in image analysis. Hyperspectral images are cubes of data, measuring spectral composition within a spatial view. As opposed to conventional three-channel color systems, the spectral information provides in-depth analysis of the composition of objects in the image scene. Since the early 1990s, hyperspectral imaging has been adopted as an airborne technique for military and environmental remote sensing and, more recently, to identify chemical species on the surface and atmosphere of Mars [1]. Hyperspectral imaging provides abundant information about ground composition, owing to an improved resolution in the spatial dimensions, with a high sensitivity in the spectral range, up to hundreds of contiguous bands covering visible- and short-wavelength infrared spectral ranges.

Even with high spatial resolution, a single pixel may consist of different materials. Spectra in a hyperspectral image can be seen as a mixing of some spectral signatures of pure physical components over the ground [2]. Despite the potential of nonlinear unmixing techniques [3], the linear mixing model has a suitable physical interpretation widely accepted within the remote sensing community. In this case, pure spectral signatures, called endmembers, are linearly combined with some abundance fractions. The key challenges for spectral unmixing are twofold: finding the collection of endmembers and estimating their abundances for each pixel in the hyperspectral image.

To identify the endmembers, early techniques were based on a predefined library of laboratory minerals, unrelated to the image under investigation [4]. Because these spectra are rarely acquired under the same conditions, this brings several difficulties in atmospheric correction and variations in the sensor intrinsic parameters. Current approaches avoid such problems by inducing the endmembers from the scene, which falls into the class of blind source separation problems (see [5] for an early study and [6] for a more recent one). Therefore, a natural tool to blind unmixing is the independent component analysis. Concerning hyperspectral data, the assumption that sources are statistically independent is violated since, due to physical constraints in the data acquisition process, the sum of the abundance fractions is constant, implying dependence among abundances [7]. Such limitations have contributed to the development of new unmixing techniques, which are roughly divided into two classes, geometric approaches and statistical ones (see [8] for a recent survey). Whereas the latter requires probabilistic foundations with some prior knowledge, the geometric approach exploits the theory of convex set. In this paper, we give particular attention to the geometric formulation. Prior to the endmember extraction, most of these techniques are never used on the original spectra. To correct the redundancy in the spectral dimension as opposed to the low number of endmembers, a dimensionality reduction transformation is often applied, such as the principal component analysis (PCA) or the minimum noise fraction (MNF).

From the linear mixing model, mixed-pixel spectra are linear mixtures of endmembers. As a consequence, they can be viewed as the vertices of a simplex enclosing all mixed spectra. Geometric techniques exploit this insight by seeking the vertices of a simplex englobing all the image data. One of the most widely used automatic endmember extraction method

is Winter's N-Findr algorithm [9]. It starts with a random set of candidate endmembers (see [10] and [11] for several implementations of N-Findr). Iteratively, one at a time, each pixel spectrum is considered as a candidate to replace each endmember. It is accepted as a new endmember if the volume of the simplex of endmembers increases. The N-Findr is a fast endmember extraction algorithm successfully applied to many hyperspectral images. Sequential algorithms can provide further reduction in computational complexity by growing the simplex gradually, vertex by vertex. The Simplex Growing Algorithm (SGA) is a sequential version of the N-Findr [12]. Starting with one vertex, it finds a simplex with the maximum volume by sequentially adding a new (optimal) vertex at a time. The Vertex Component Analysis (VCA) algorithm is another sequential algorithm [13]. It exploits the fact that the orthogonal subspace projection (OSP) of a simplex is also a simplex, and thus, vertices of the latter are vertices of the initial one. The VCA gradually selects vertices by performing OSPs, sequentially starting from a 1-D subspace. The Iterated Constrained Endmembers (ICE) algorithm fits an enclosing simplex to the data cloud while penalizing its volume [14]. To this end, an alternating optimization scheme is used by minimizing, on the one hand, a quadratic cost function for fitness and, on the other hand, the distance between endmembers for penalization. A sparsity-promoting version of ICE is presented in [15].

Two physical constraints are generally imposed on the linear mixing model, enforcing constraints on the fractional abundances for each pixel: 1) the sum-to-one (or equality) constraint, which indicates that the endmember contribution must add up to 100%, and 2) the nonnegativity constraint, since negative contributions are physically unrealistic. The most straightforward approach to estimate abundances is by an unconstrained least-squares minimization, with the abundances of a given pixel determined by a matrix inversion [16]. For each pixel, the computational complexity is cubic in the number of endmembers. The sum-to-one constraint can be imposed to the least-squares solution using, for instance, Lagrangian multipliers. The nonnegativity constraint is more difficult to address, since it does not have a closed-form solution. Many iterative approaches have been proposed to this end, including nonnegative matrix factorization techniques [17], [18], as well as general iterative techniques [19], [20]. A fully constrained solution requires more advanced optimization methods [21], [22]. Solutions to these problems involve computational extensive algorithms, which are not appropriate for a large number of hyperspectral pixels (for implementation issues, see, for instance, [23] and [24]). It is worth noting that if the endmembers were properly identified, i.e., the vertices of a simplex englobing all the data, both sum-to-one and nonnegativity constraints would be naturally fulfilled. For this reason, extraction techniques often directly apply the unconstrained least-squares method [9], [13], [25].

In this paper, we give a geometric formulation to solve the abundance estimation problem. To this end, we redefine the fractional abundances as barycentric coordinates (or areal coordinates) in the reduced dimensional space. We derive two expressions of these coordinates, either as a volume ratio of simplexes or as a ratio of distances. It is amazing to observe

that these volumes and distances are often computed by well-known endmember extraction methods in order to identify the endmembers. This is the case of N-Findr and SGA algorithms, which compute volumes, whereas VCA and ICE estimate distances. By taking advantage of this situation, we show that one can easily incorporate abundance estimation within conventional endmember extraction techniques, without essentially incurring additional computational cost.

The remainder of this paper is organized as follows. In Section II, we present barycentric coordinates for the estimation of fractional abundances. In Section III, we demonstrate that our approach is natural to many endmember extraction techniques and we outline its application to N-Findr, SGA, VCA, and ICE. The effectiveness of the method is illustrated in Section IV by comparing it to the fully constrained least-squares solution. Finally, Section V summarizes this work and describes ongoing efforts. However, first, we give a mathematical formulation of the linear mixing/unmixing model.

A. Linear Mixing/Unmixing Model

Given a hyperspectral image, let $\boldsymbol{x}_\ell$ be the spectrum of the ℓ-th pixel, with each pixel indexed using a single index. The linear mixing model takes the form

$$\boldsymbol{x}_\ell = \sum_{i=1}^{n} \alpha_i \boldsymbol{x}_{\omega_i} \qquad (1)$$

where $\{\boldsymbol{x}_{\omega_1}, \boldsymbol{x}_{\omega_2}, \dots, \boldsymbol{x}_{\omega_n}\}$ denotes the collection of the n endmembers. In matrix form, the linear mixing model is given by

$$\boldsymbol{x}_\ell = \boldsymbol{X}\boldsymbol{\alpha} \qquad (2)$$

where $\boldsymbol{X} = [\boldsymbol{x}_{\omega_1}\,\boldsymbol{x}_{\omega_2}\ldots\boldsymbol{x}_{\omega_n}]$ and $\boldsymbol{\alpha} = [\alpha_1\,\alpha_2\ldots\alpha_n]^\top$ are the vectors of the abundances to be determined. We suppose for now that the endmembers have been identified using any off-the-shelf endmember extraction technique.

The fractional abundance α_i represents the contribution in $\boldsymbol{x}_\ell$ of the pure material defined by $\boldsymbol{x}_{\omega_i}$. In order to adopt a physical interpretation of this mixing model, the abundances must satisfy two constraints:

1) the sum-to-one constraint (also called the equality constraint) with

$$\sum_{i=1}^{n} \alpha_i = 1$$

2) the nonnegativity constraint with

$$\alpha_1, \alpha_2, \dots, \alpha_n \geq 0.$$

These constraints can be written in matrix form as $\mathbf{1}^\top\boldsymbol{\alpha} = 1$ and $\boldsymbol{\alpha} \geq 0$, where $\mathbf{1}$ is the unit column vector of n entries and the inequality is taken componentwise.

Ignoring these constraints, the optimal solution of the problem (2), with optimality in the least-squares sense, is given by the normal equation

$$\boldsymbol{\alpha}_{\mathrm{LS}} = (\boldsymbol{X}^\top\boldsymbol{X})^{-1}\boldsymbol{X}^\top\boldsymbol{x}_\ell. \qquad (3)$$

The equality constraint is the simplest constraint to enforce and can be incorporated by using Lagrangian multipliers, resulting into the optimal solution

$$\boldsymbol{\alpha}_{\text{eqLS}} = \boldsymbol{\alpha}_{\text{LS}} - \frac{1}{\mathbf{1}^\top (\boldsymbol{X}^\top \boldsymbol{X})^{-1} \mathbf{1}} (\boldsymbol{X}^\top \boldsymbol{X})^{-1} \mathbf{1} (\mathbf{1}^\top \boldsymbol{\alpha}_{\text{LS}} - 1). \quad (4)$$

Enforcing the nonnegativity constraint is not as easy to address as the equality constraint since no closed-form solution exists. In the least-squares sense, the problem consists of minimizing $f(\boldsymbol{\alpha}) = (1/2)\|\boldsymbol{x}_\ell - \boldsymbol{X}\boldsymbol{\alpha}\|^2$ while maintaining $\boldsymbol{\alpha} \geq 0$. Let $\nabla f(\boldsymbol{\alpha}) = \boldsymbol{X}^\top (\boldsymbol{X}\boldsymbol{\alpha} - \boldsymbol{x}_\ell)$ denote the gradient of $f(\boldsymbol{\alpha})$. Then, the Karush–Kuhn–Tucker optimality conditions [26] for this problem are $\boldsymbol{\alpha} \geq 0$, $\nabla f(\boldsymbol{\alpha}) \geq 0$, and $\nabla f(\boldsymbol{\alpha})^\top \boldsymbol{\alpha} = 0$. This can be solved using iterative techniques, such as an alternating strategy applied to both expressions

$$\boldsymbol{\alpha}^\top \boldsymbol{X}^\top (\boldsymbol{X}\boldsymbol{\alpha} - \boldsymbol{x}_\ell) = 0, \quad \text{and} \quad \boldsymbol{\alpha} \geq 0. \quad (5)$$

The most commonly used algorithm to compute the solution is the Lawson–Hanson algorithm [19], which uses the *active set* scheme. Other iterative algorithms include multiplicative iterative strategies [20]. The problem of estimating the abundances using the linear model subject to both equality and nonnegativity constraints, the so-called fully constrained solution, requires advanced iterative optimization methods [21]. All these solutions are optimal, in the least-squares sense, and can be considered even when the number of bands (dimension) is greater than the number of endmembers.

In practice, the spectral dimension is reduced to $n - 1$ in order to have the mixing model (1) satisfied. Such representations allow the extraction of the endmembers. We shall now give a direct geometric formalism to estimate the abundances in the same low-dimensional representation. To this end, we solve the equality-constrained optimization problem geometrically and give a straightforward interpretation to the violation of the nonnegativity constraint.

II. BARYCENTRIC COORDINATES FOR ABUNDANCE ESTIMATION

Suppose, for now, that the endmembers have been extracted using, for instance, any of the aforementioned techniques, such as N-Findr or SGA algorithms. We seek to estimate the abundances, i.e., $\alpha_1, \alpha_2, \ldots, \alpha_n$, for each spectrum in the image. Given any $\boldsymbol{x}_\ell$, we consider the linear mixing model with the equality constraint, namely

$$\boldsymbol{x}_\ell = \sum_{i=1}^{n} \alpha_i \boldsymbol{x}_{\omega_i} \quad (6)$$

subject to

$$\sum_{i=1}^{n} \alpha_i = 1. \quad (7)$$

Since both are equality expressions, we combine them into a single matrix expression, with the augmented linear system

$$\begin{bmatrix} 1 & 1 & \cdots & 1 \\ \boldsymbol{x}_{\omega_1} & \boldsymbol{x}_{\omega_2} & \cdots & \boldsymbol{x}_{\omega_n} \end{bmatrix} [\alpha] = \begin{bmatrix} 1 \\ \boldsymbol{x}_\ell \end{bmatrix}. \quad (8)$$

It is worth noting that this is a linear system with as many equations as unknowns, i.e., n. Linear algebra provides many elegant methods to solve such systems [16].

We propose to solve this problem using Cramer's rule [16, p. 259]. The consequences of this choice will be clear throughout this paper. Cramer's rule states that the solution of a linear system can be expressed in terms of the determinants of the system matrix and of the matrices obtained from it with one column substituted by the right-hand-side vector. With this rule applied to the aforementioned augmented linear system (8), the solution can be written as

$$\alpha_1 = \frac{\det \begin{bmatrix} 1 & 1 & \cdots & 1 \\ \boldsymbol{x}_\ell & \boldsymbol{x}_{\omega_2} & \cdots & \boldsymbol{x}_{\omega_n} \end{bmatrix}}{\det \begin{bmatrix} 1 & 1 & \cdots & 1 \\ \boldsymbol{x}_{\omega_1} & \boldsymbol{x}_{\omega_2} & \cdots & \boldsymbol{x}_{\omega_n} \end{bmatrix}}$$

$$\alpha_2 = \frac{\det \begin{bmatrix} 1 & 1 & \cdots & 1 \\ \boldsymbol{x}_{\omega_1} & \boldsymbol{x}_\ell & \cdots & \boldsymbol{x}_{\omega_n} \end{bmatrix}}{\det \begin{bmatrix} 1 & 1 & \cdots & 1 \\ \boldsymbol{x}_{\omega_1} & \boldsymbol{x}_{\omega_2} & \cdots & \boldsymbol{x}_{\omega_n} \end{bmatrix}},$$

$$\vdots$$

$$\alpha_n = \frac{\det \begin{bmatrix} 1 & 1 & \cdots & 1 \\ \boldsymbol{x}_{\omega_1} & \boldsymbol{x}_{\omega_2} & \cdots & \boldsymbol{x}_\ell \end{bmatrix}}{\det \begin{bmatrix} 1 & 1 & \cdots & 1 \\ \boldsymbol{x}_{\omega_1} & \boldsymbol{x}_{\omega_2} & \cdots & \boldsymbol{x}_{\omega_n} \end{bmatrix}} \quad (9)$$

where det is the determinant operator. The amazing thing about Cramer's rule is that one only needs to compute the determinants in order to solve a linear system, as opposed to conventional matrix inversion techniques. In fact, both methods are equivalent. Moreover, when the rule is applied to the proposed augmented linear system, we get an intuitive geometric interpretation, natural in the context of simplexes with vertices defined by hyperspectral data.

A. Geometric Formulation

Now, we recall the expression of the volume of a simplex. Let $\boldsymbol{X} = \{\boldsymbol{x}_{\omega_1}, \boldsymbol{x}_{\omega_2}, \ldots, \boldsymbol{x}_{\omega_n}\}$ be the set of linearly independent vectors in an $(n - 1)$-dimensional space, thus defining a nondegenerated simplex in that space. This assumption is true in the case of endmembers. We define the *oriented* volume of the simplex with vertices $\boldsymbol{X}$, as follows:

$$\mathcal{V}_{\boldsymbol{X}} = \frac{1}{(n-1)!} \det \begin{bmatrix} 1 & 1 & \cdots & 1 \\ \boldsymbol{x}_{\omega_1} & \boldsymbol{x}_{\omega_2} & \cdots & \boldsymbol{x}_{\omega_n} \end{bmatrix}. \quad (10)$$

This expression gives a signed value, either positive or negative depending on the order of the simplex vertices, i.e.,
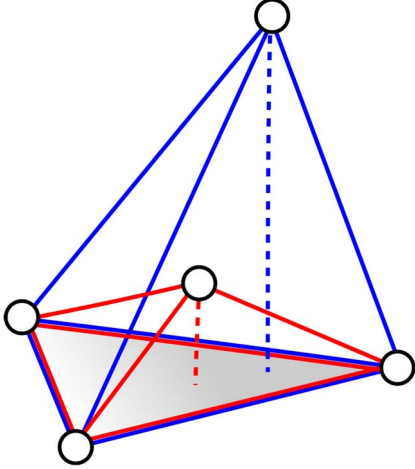
Fig. 1.   Volume of a tetrahedron (3-D simplex) is given by the third of the area of the base times the height from the base to the apex. Since both (blue and red) tetrahedrons share the same (gray) base, the ratios of their volumes are proportional to the (dashed lines) ratios of their heights.

the sequence $\boldsymbol{x}_{\omega_1}, \boldsymbol{x}_{\omega_2}, \ldots, \boldsymbol{x}_{\omega_n}$. The consequences of the use of the oriented (signed) volume, rather than the use of the conventional positive-valued expression $|\mathcal{V}_{\boldsymbol{x}}|$, will be justified.

Let $\setminus$ denote the set difference operator, with $\boldsymbol{X} \setminus \{\boldsymbol{x}_{\omega_i}\} \cup \{\boldsymbol{x}_\ell\}$ as the set defined by set $\boldsymbol{X}$, where $\boldsymbol{x}_{\omega_i}$ has been removed and $\boldsymbol{x}_\ell$ added. From Cramer's rule (9), each coefficient α_i can be written as a ratio of two oriented volumes of simplexes, namely, on the one hand, the simplex with vertices $\boldsymbol{X}$ given by the endmembers and, on the other hand, the same simplex with $\boldsymbol{x}_{\omega_i}$ replaced by $\boldsymbol{x}_\ell$. In a compact form, we have

$$\alpha_i = \frac{\mathcal{V}_{\boldsymbol{X} \setminus \{\boldsymbol{x}_{\omega_i}\} \cup \{\boldsymbol{x}_\ell\}}}{\mathcal{V}_{\boldsymbol{X}}} \tag{11}$$

for all $i = 1, 2, \ldots, n$. As shown below, these volumes are often computed by the endmember extraction techniques, as in the case of the N-Findr algorithm, for instance. Therefore, one can estimate abundances with essentially no computational cost.

B. Distance-Based Formulation

All the abundances can be estimated using (11) or, equivalently, from (9). This illustrates the fact that, for each abundance, the two considered simplexes have $n - 1$ identical vertices and only one different vertex $\boldsymbol{x}_{\omega_i}$, which has been substituted in the numerator by $\boldsymbol{x}_\ell$. Since these $n - 1$ vertices provide a common *base* for both simplexes, we can further simplify the expression (11) (see Fig. 1 for a 3-D illustration). In fact, remember that the volume of a simplex of n vertices can be given in terms of the content (length, area, volume, ...) of a *base* of $n - 1$ vertices and the distance of the remaining vertex to the subspace including the base, that is, we have

$$\mathcal{V}_{\boldsymbol{X}} = \frac{1}{n - 1} \delta\left(\boldsymbol{x}_{\omega_i}\right) \mathcal{V}_{\boldsymbol{X} \setminus \{\boldsymbol{x}_{\omega_i}\}}$$

where $\delta(\boldsymbol{x}_{\omega_i})$ is the (signed) distance between the vertex $\boldsymbol{x}_{\omega_i}$ and the subspace spanned by the other vertices in $\boldsymbol{X}$. By using this notation, we get

$$\alpha_i = \frac{\delta(\boldsymbol{x}_\ell)}{\delta\left(\boldsymbol{x}_{\omega_i}\right)} \tag{12}$$

for all $i = 1, 2, \ldots, n$. This formulation is more adapted to incremental endmember extraction techniques, as opposed to the volume ratio in (11). This is mainly due to the fact that this expression does not require explicit relations between previously selected endmembers. Only distances to the subspace spanned by the latter are considered. This results in low computational complexity algorithms, as illustrated, for instance, with the VCA.

C. On the Nonnegativity Constraint

As defined earlier, the oriented volume of a simplex can be either positive or negative, depending on the order of the sequence defined by its vertices. In order to study the sign of any coefficient α_i, we need to compare the volumes in (11) or, equivalently, the corresponding determinants. The only difference resides in one column, the ith column, which is either $\boldsymbol{x}_{\omega_i}$ or $\boldsymbol{x}_\ell$. Therefore, one only needs to compare the orientation of these simplexes. If both simplexes have the same orientation, the coefficient is positive; otherwise, when they have opposite orientations, it is negative.

To illustrate this point, we consider the 2-D example in Fig. 2. Consider that the first coefficient is given by $\alpha_1 = \mathcal{V}_{\boldsymbol{X} \setminus \{\boldsymbol{x}_{\omega_1}\} \cup \{\boldsymbol{x}_\ell\}} / \mathcal{V}_{\boldsymbol{X}}$. Therefore, we compare the simplexes $\boldsymbol{X} = \{\boldsymbol{x}_{\omega_1}, \boldsymbol{x}_{\omega_2}, \boldsymbol{x}_{\omega_3}\}$ and $\{\boldsymbol{x}_\ell, \boldsymbol{x}_{\omega_2}, \boldsymbol{x}_{\omega_3}\}$. Fig. 2 (left) shows the case where both simplexes have the same orientation, i.e., counterclockwise in the sequences $\boldsymbol{x}_{\omega_1} \boldsymbol{x}_{\omega_2} \boldsymbol{x}_{\omega_3}$ and $\boldsymbol{x}_\ell \boldsymbol{x}_{\omega_2} \boldsymbol{x}_{\omega_3}$. In this case, α_1 is nonnegative. Fig. 2 (right) shows the case of opposite orientations, with a clockwise orientation in the sequence $\boldsymbol{x}_\ell \boldsymbol{x}_{\omega_2} \boldsymbol{x}_{\omega_3}$ as opposed to the counterclockwise in $\boldsymbol{x}_{\omega_1} \boldsymbol{x}_{\omega_2} \boldsymbol{x}_{\omega_3}$. This results in $\alpha_1 < 0$. Applying the same argument for the other coefficients, we find that α_2 and α_3 are nonnegative in both cases (left and right figures).

Now, consider the signed distances in (12). As shown in Fig. 3, $\boldsymbol{x}_{\omega_2} \boldsymbol{x}_{\omega_3}$ divides $\mathbb{R}^2$ into two regions. Coefficient α_1 is positive if both $\boldsymbol{x}_\ell$ and $\boldsymbol{x}_{\omega_1}$ lie on the same side (left figure). Otherwise, it is negative (right figure).

The results obtained for all the coefficients are in accordance with the definition of a convex hull, indicating that $\boldsymbol{x}_\ell$ is inside the simplex if and only if all the α_is are nonnegative. Moreover, we can derive a simple inclusion test as follows: $\boldsymbol{x}_\ell$ is inside the simplex if and only if all the determinants in (9) have the same sign (either positive or negative); otherwise, if it is outside, there exists at least one determinant with an opposite sign. This provides an elegant inclusion test, where only determinant evaluation is required, a step carried out by the endmember extraction stage, as derived in the next section.

It is worth noting that the nonnegativity constraints are not imposed in the proposed method. However, the violation of these constraints, i.e., the existence of at least one negative α_i,
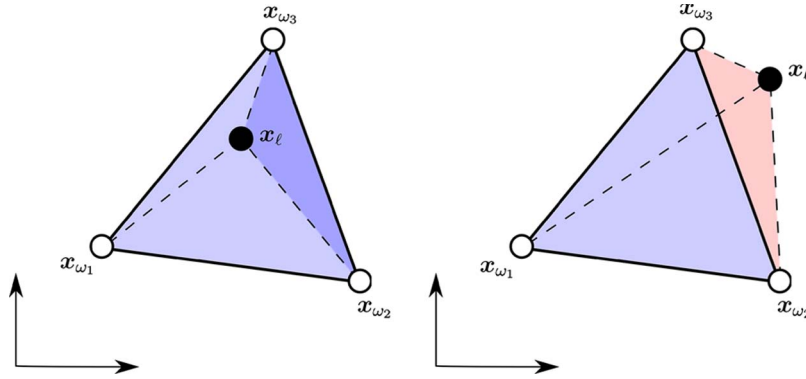
Fig. 2. Illustration of the (triangle) simplex in a 2-D Euclidean space to study the sign of the coefficient α_1. In the left figure, x_ℓ and x_{ω_1} are on the same side of the line defined by x_{ω_2} and x_{ω_3}; thus, α_1 is nonnegative. In the right figure, α_1 is negative since they lie on opposite sides.
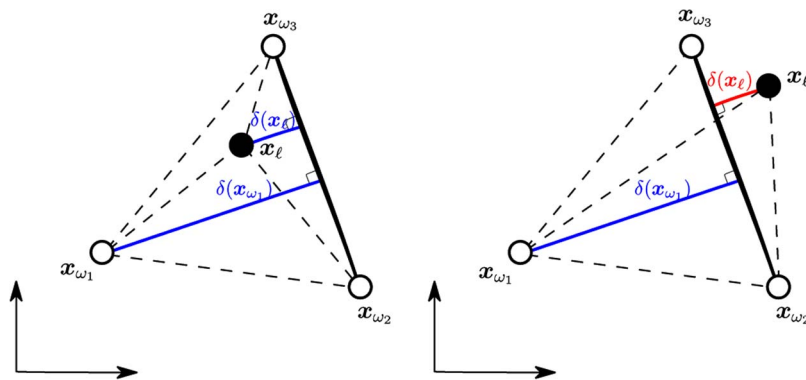
Fig. 3. Two-dimensional illustration of α_1 computation using the heights. In this case, $\alpha_1 = \delta(x_\ell)/\delta(x_{\omega_1})$. In the left figure, x_ℓ and x_{ω_1} are on the same side of the line, defined by x_{ω_2} and x_{ω_3}, and α_1 is nonnegative. In the right figure, α_1 is negative since x_ℓ and x_{ω_1} lie on both sides.

means that x_ℓ is outside the simplex. Such a result implies that both equality and nonnegativity constraints cannot be satisfied by the resulting linear combination of endmembers. This illustrates the limitations of geometric approaches for endmember extraction (described hereafter) in properly identifying the endmembers.[1]

---

[1]Such a result is also related to the uniqueness of the unmixing solution (or the endmember identifiability condition, as given in [27, Theorem 1]). In fact, let $x_{\ell_1}, x_{\ell_2}, \ldots, x_{\ell_n}$ be the spectra corresponding to some arbitrary pixels. Then, we have, from (8)

$$\begin{bmatrix} 1 & \cdots & 1 \\ x_{\ell_1} & \cdots & x_{\ell_n} \end{bmatrix} = \begin{bmatrix} 1 & \cdots & 1 \\ x_{\omega_1} & \cdots & x_{\omega_n} \end{bmatrix} \begin{bmatrix} \alpha_{\ell_1} & \cdots & \alpha_{\ell_n} \end{bmatrix}$$

where the equality also holds for the volumes as defined in (10), namely

$$\left| \mathcal{V}_{\{x_{\ell_1}, \ldots, x_{\ell_n}\}} \right| = \left| \mathcal{V}_{\{x_{\omega_1}, \ldots, x_{\omega_n}\}} \right| \left| \det \begin{bmatrix} \alpha_{\ell_1} & \cdots & \alpha_{\ell_n} \end{bmatrix} \right|.$$

The determinant in this expression can be upper bounded using Hadamard's inequality, with

$$\left| \det \begin{bmatrix} \alpha_{\ell_1} & \cdots & \alpha_{\ell_n} \end{bmatrix} \right| \leq \prod_{j=1}^{n} \left\| \alpha_{\ell_j} \right\|$$

where the inequality becomes an equality when the matrix is a permutation matrix. If the sum-to-one and the nonnegativity constraints are satisfied, then this upper bound equals 1. Therefore, the volume of the simplex defined by any arbitrary set cannot be greater than the one defined by the endmembers.

III. ABUNDANCE ESTIMATION USING STATE-OF-THE-ART ENDMEMBER EXTRACTION TECHNIQUES

Many endmember extraction techniques determine endmembers as vertices of a simplex englobing all the spectra. In this section, we show how one can easily take advantage of some of these techniques in order to estimate the abundances using barycentric coordinates. To keep the presentation as simple as possible, we restrict ourselves to classical well-known techniques.

A. N-Findr Algorithm

The N-Findr algorithm seeks the simplex with the largest volume in an iterative manner by visiting each pixel to inflate the simplex. In a preprocessing stage, a dimensionality reduction method, such as PCA or MNF, is applied to get data into an $(n-1)$-dimensional space, with n being the number of endmembers. At initialization, an initial set of n endmember candidates is selected randomly.[2] Let $X = \{x_{\omega_1}, x_{\omega_2}, \ldots, x_{\omega_n}\}$ be the set of corresponding spectra.

---

[2]The initial set influences the resulting endmembers and, therefore, the estimated abundances. More efficient selection techniques may also be applied to construct the initial set. See, e.g., [28]. We keep the exposition clear with the original N-Findr algorithm.
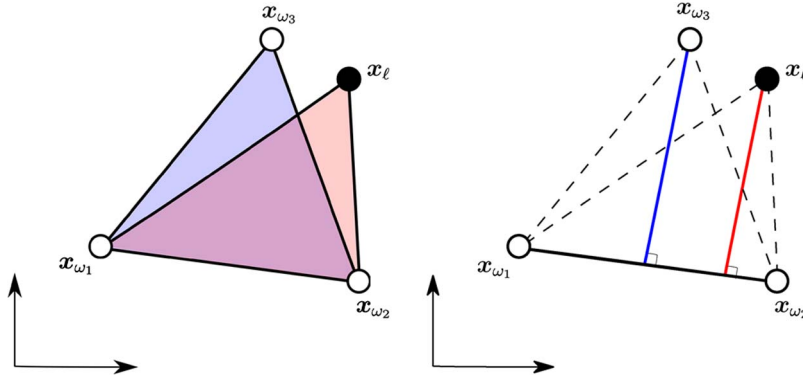
Fig. 4.   Illustration of endmember extraction incremental algorithms in a 2-D Euclidean space. From two previously extracted endmembers, $\boldsymbol{x}_{\omega_1}$ and $\boldsymbol{x}_{\omega_2}$, the third endmember is determined (left) using SGA by comparing simplex volumes or (right) using VCA by comparing distances to the subspace spanned by previous endmembers. The abundance α_3 is given by (left) the ratio of volumes or (right) the ratio of distances.

The following process is iterated for each pixel, with $\boldsymbol{x}_\ell$ being its spectrum. One at a time, each endmember is replaced by the spectrum under investigation and the oriented[3] volume of the resulting simplex is evaluated. We get n new volumes, $\mathcal{V}_{\boldsymbol{X}\setminus\{\boldsymbol{x}_{\omega_i}\}\cup\{\boldsymbol{x}_\ell\}}$, as well as the initial volume $\mathcal{V}_{\boldsymbol{X}}$. Comparing these volumes, we get the following decision rule.

1) If the tested volumes are less than the initial one, in absolute values, namely, $\max_i |\mathcal{V}_{\boldsymbol{X}\setminus\{\boldsymbol{x}_{\omega_i}\}\cup\{\boldsymbol{x}_\ell\}}| < |\mathcal{V}_{\boldsymbol{X}}|$, then the initial set of endmembers remains unchanged.

2) Otherwise, in order to inflate the volume, some entry of the endmember set is replaced by $\boldsymbol{x}_\ell$. The outgoing spectrum $\boldsymbol{x}_{\omega_i}$ is identified as follows: $\omega_i = \arg\max |\mathcal{V}_{\boldsymbol{X}\setminus\{\boldsymbol{x}_{\omega_i}\}\cup\{\boldsymbol{x}_\ell\}}|$.

It turns out that the volumes already computed for endmember extraction can be used to estimate the abundances using (11), namely, by defining the contribution of $\boldsymbol{x}_{\omega_i}$ in $\boldsymbol{x}_\ell$ by

$$\alpha_i = \frac{\mathcal{V}_{\boldsymbol{X}\setminus\{\boldsymbol{x}_{\omega_i}\}\cup\{\boldsymbol{x}_\ell\}}}{\mathcal{V}_{\boldsymbol{X}}}.$$

As given in this expression, the contribution of any endmember requires only an arithmetic division for each pixel. Therefore, estimating all the abundances for all the pixels can be done with a simple arithmetic division applied nN times.

B. SGA

The SGA improves the N-Findr in two main aspects: 1) At initialization, the starting set is not randomly selected, and 2) the simplex is growing one endmember at a time until all endmembers are extracted.

At initialization, a single dimension is considered, using, for instance, PCA, where a simplex is a nontrivial line segment. The first endmember $\boldsymbol{x}_{\omega_1}$ is determined by maximizing $|\mathcal{V}_{\{\boldsymbol{x}_{\omega_1},\boldsymbol{x}_0\}}|$, where $\boldsymbol{x}_0$ is randomly selected. Iteratively, the

endmembers are extracted one at a time. At step i for $2 \leq i \leq n$, with the dimensionality reduced to $i - 1$, the ith endmember is determined by the index ω_i as follows:

$$\omega_i = \arg\max_\ell |\mathcal{V}_{\boldsymbol{X}\cup\{\boldsymbol{x}_\ell\}}|$$

where $\boldsymbol{X}$ corresponds to the set of endmembers previously extracted. This is shown in Fig. 4 (right).

In the same way as the N-Findr, the volumes computed by the SGA allow the estimation of the abundances, as given by (11). The difference resides in that, at a given step i, the computed volumes give the contributions of ω_i in all $\boldsymbol{x}_\ell$ in the $(i-1)$-dimensional space and not in the final $(n-1)$-dimensional space defined by the n-order mixing model.

C. VCA

The VCA exploits the fact that an affine transformation of a simplex is also a simplex, particularly by projection operation. The incremental scheme projects the data onto a direction orthogonal to the subspace spanned by previously selected endmembers. The extreme of this projection specifies the new endmember. The algorithm iterates until it reaches the desired number of endmembers.

Roughly speaking, the VCA considers the distance of candidate data to the subspace spanned by the endmembers already determined. The new endmember corresponds to the farthest data, as shown in Fig. 4 (left). It turns out that these distances are the same as those introduced in (12) and, consequently, allow us to estimate abundances as follows:

$$\alpha_3 = \frac{\delta(\boldsymbol{x}_\ell)}{\delta(\boldsymbol{x}_{\omega_3})}.$$

Once again, only one arithmetic division is required to estimate the contribution of any endmember for each pixel. Moreover, the VCA selection criteria, i.e., $\boldsymbol{x}_{\omega_3} = \arg\max_{\boldsymbol{x}_\ell} \delta(\boldsymbol{x}_\ell)$, gives a natural framework for both equality and nonnegativity constraints. If there exists some $\boldsymbol{x}_\ell$ such that $\delta(\boldsymbol{x}_{\omega_3}) < \delta(\boldsymbol{x}_\ell)$, then

---

[3]The original algorithm uses a positive-valued volume, here recasted into a signed one. Although this turns out to be very useful, the algorithm remains essentially the same.

from the aforementioned expression, $\alpha_3 > 1$, and consequently, the constraints are violated.

D. Connections to the ICE Method

The ICE method seeks the simplex englobing the data by minimizing the residuals in a least-squares sense. Essentially, the algorithm minimizes, on the one hand, the mean squared error

$$\frac{1}{N} \sum_{\ell=1}^{N} \left\| \boldsymbol{x}_\ell - \sum_{i=1}^{n} \alpha_i \boldsymbol{x}_{\omega_i} \right\|^2$$

and, on the other, the sum of squared distances between all endmembers, namely

$$\sum_{\substack{i \neq j \\ i,j=1}}^{n} \left\| \boldsymbol{x}_{\omega_i} - \boldsymbol{x}_{\omega_j} \right\|^2 .$$

The former enlarges the simplex englobing the data, whereas the latter constrains its volume. ICE uses an alternating minimization scheme to extract endmembers (from a quadratic objective function) and estimate their contributions (solving a quadratic programming problem).

The ICE method considers (squared) distances between all couples of data, endmembers and non-endmembers. Using the distances between vertices of a simplex, we can easily compute its volume, owing to the Cayley–Menger determinants [29]. The square volume of a simplex in an $(n-1)$-dimensional space is given by

$$\mathcal{V}_{\boldsymbol{X}}^2 = c_{n-1} \det \begin{bmatrix} 0 & 1 & 1 & 1 & \cdots & 1 \\ 1 & 0 & \delta_{1,2}^2 & \delta_{1,3}^2 & \cdots & \delta_{1,n}^2 \\ 1 & \delta_{2,1}^2 & 0 & \delta_{2,3}^2 & \cdots & \delta_{2,n}^2 \\ 1 & \delta_{3,1}^2 & \delta_{3,2}^2 & 0 & \cdots & \delta_{3,n}^2 \\ \vdots & \vdots & \vdots & \vdots & \ddots & \vdots \\ 1 & \delta_{n,1}^2 & \delta_{n,2}^2 & \delta_{n,3}^2 & \cdots & 0 \end{bmatrix}$$

where $\delta_{i,j}$ denotes the distance between two vertices and $c_n = (-1)^{n+1}/2^n(n!)^2$.

Whereas the Cayley–Menger expression computes the determinant of an $(n+1)$-by-$(n+1)$ matrix, its particular form results in a lower computational cost. To show this, consider the case of $n-1=2$ dimensions. Then, the Cayley–Menger determinant leads to Heron's formula of triangles, with $\mathcal{V}_{\boldsymbol{X}}^2 = 1/16(\delta_{1,2} + \delta_{1,3} + \delta_{2,3})(\delta_{1,2} + \delta_{1,3} - \delta_{2,3})(\delta_{1,2} - \delta_{1,3} + \delta_{2,3})(-\delta_{1,2} + \delta_{1,3} + \delta_{2,3})$, where only four arithmetic multiplications are required.

E. Connection to Subspace Projection Techniques

The OSP method is a general technique for detection, discrimination, and classification in hyperspectral imaging [30]. When this method is applied for endmember extraction, the
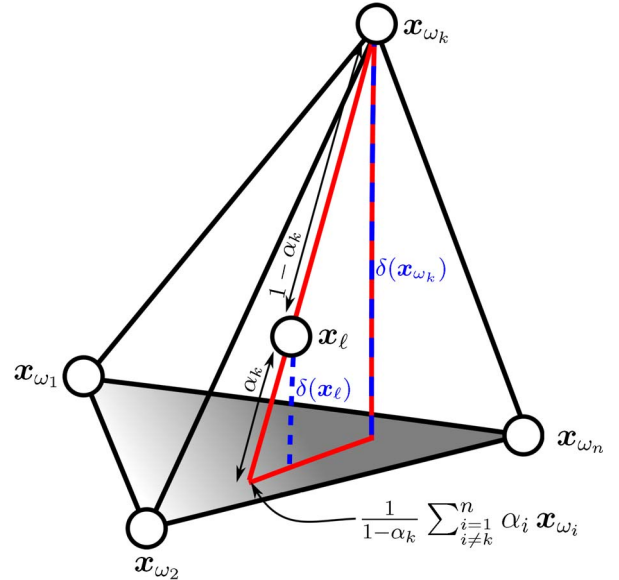

Fig. 5. By applying the intercept theorem for the (blue) two dashed lines in the (red) triangle, we get $\alpha_k = \delta(\boldsymbol{x}_\ell)/\delta(\boldsymbol{x}_{\omega_k})$.

abundances are often given using a least-squares estimate [31]. It is described by writing (1) as

$$\boldsymbol{x}_\ell = \alpha_k \boldsymbol{x}_{\omega_k} + \sum_{\substack{i=1 \\ i \neq k}}^{n} \alpha_i \boldsymbol{x}_{\omega_i}$$

for any $k = 1, 2, \ldots, n$. To extract $\boldsymbol{x}_{\omega_k}$, an operator (matrix) is designed to annihilate the second term in the right-hand side. By letting $\boldsymbol{U} = \boldsymbol{X} \setminus \{\boldsymbol{x}_{\omega_k}\}$, one can consider the projection operator

$$\boldsymbol{I} - \boldsymbol{U}(\boldsymbol{U}^\top \boldsymbol{U})^{-1} \boldsymbol{U}^\top. \tag{13}$$

This operator projects the data into the null space of $\boldsymbol{U}$, as shown in [32]. In [33], the abundances are estimated using a geometric point of view in the same way as the barycentric approach proposed in this paper. The connection between both techniques is shown in Fig. 5 where, by applying the intercept theorem, one obtains (12), namely

$$\alpha_k = \frac{\delta(\boldsymbol{x}_\ell)}{\delta(\boldsymbol{x}_{\omega_k})}.$$

It is worth noting that our method does not require any matrix inversion, as opposed to subspace projection techniques, as shown in (13).

IV. EXPERIMENTATIONS

In this section, we study the relevance of the proposed abundance estimation scheme. To this end, we compare it to the results obtained with the least-squares solutions, the unconstrained (3), the equality-constrained (4), the nonnegativity constraint (5), and the fully constrained [21] solutions. We
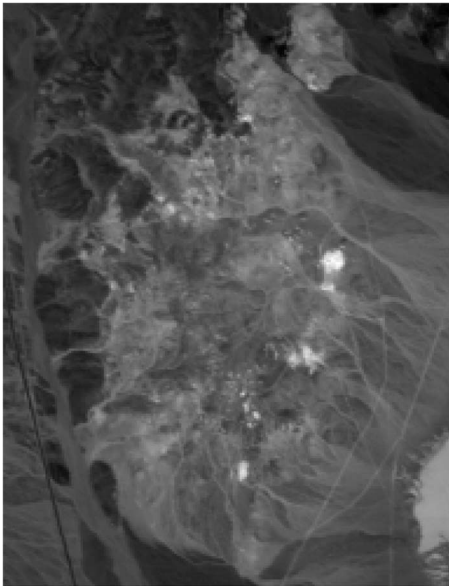
Fig. 6. AVIRIS Cuprite Nevada hyperspectral subimage at a wavelength of 1.3 μm (band 100).
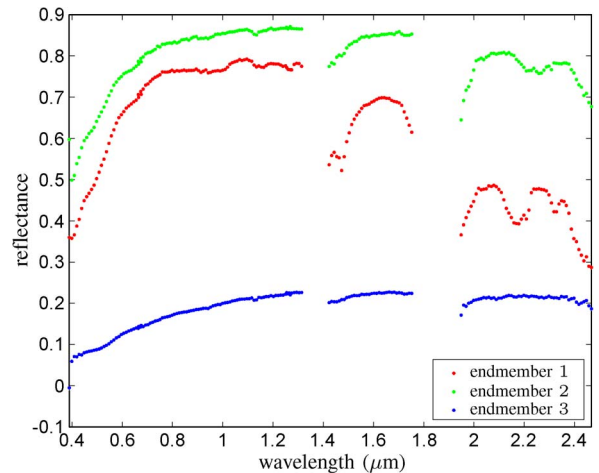

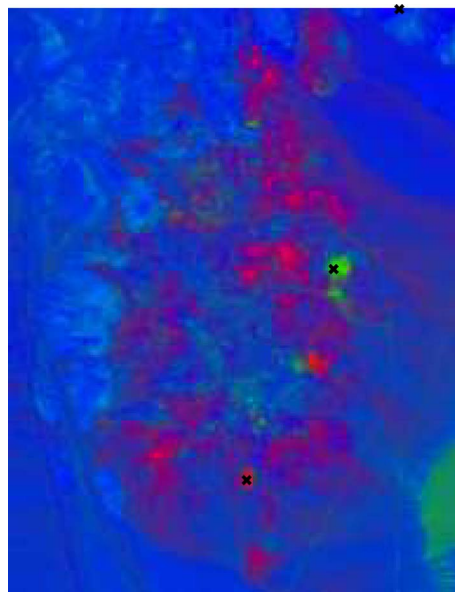Fig. 7. Three extracted endmembers, mainly representing Alunite, Kaolinite, and Sphene.

Fig. 8. Three-channel color composite, with ● red, ● green, and ● blue for the first, second, and third extracted endmembers, respectively. The location of each endmember, indicated by **x**, is consistent with ground truth measurements.

emphasize on the fact that all these least-squares solutions are computed from the spectral data, without any dimension reduction, as opposed to our approach which exploits the PCA (or MNF) representation, which is already computed for endmember extraction. As we work in a lower dimension, one should expect to have lower performance.

The study of the optimality of the dimensionality reduction technique and of the endmember extraction method are beyond the scope of this paper.

A. Real Hyperspectral Image

The studied hyperspectral image is the scene of the Cuprite mining district in western Nevada, U.S., captured by NASA's Airborne Visible/Infrared Imaging Spectrometer (AVIRIS). Over the past years, this site has been extensively studied by the remote sensing community [34], providing a high-accuracy ground truth map [35], [36]. The AVIRIS sensor collects 224 contiguous spectral bands covering wavelengths ranging from 0.38 to 2.5 μm, with a spectral resolution of approximately 0.01 μm. Atmospheric correction is applied (removing bands 1–2, 104–113, 148–167, and 221–224), which yields a total of 188 bands. Previously studied in [13] and [37] for endmember extraction, the subimage consists of 250 lines of 191 pixels each, as shown in Fig. 6.

In the experiments, we used N-Findr to extract the endmembers, set in this paper to $n = 3$ for illustration purposes (the 2-D representation and RGB map are presented later in this paper). This is not the optimal number of endmembers for this image, with an estimated virtual dimensionality equal to 12 as studied in [13] or 9 for almost the same scene in [37]. The identified endmembers are the first three endmembers obtained from the VCA, namely, Alunite, Kaolinite, and Sphene, a result conforming to the ground truth information. The spectra of these endmembers are shown in Fig. 7.

We applied barycentric coordinates, i.e., using (11), to estimate the abundances of these endmembers within the hyperspectral image. These results are shown on the map in Fig. 8, using a three-channel color composite, with red, green, and blue for the first, second, and third extracted endmembers, respectively. With both the endmember extraction and the abundance estimation operated in the 2-D space given by the PCA, we represented the data in Fig. 9. With 30% of the data outside the simplex defined by these endmembers, 14 586 data (out of 47 750) violated the nonnegativity constraint, with at least one estimated negative α_i. The spatial distribution of the pixels violating the nonnegativity constraint indicate the specific areas where the linear model does not hold (see, for instance, [1] and [38]). As shown in Fig. 10, where the largest negative α_is are shown (pixels with zero value correspond to pixels
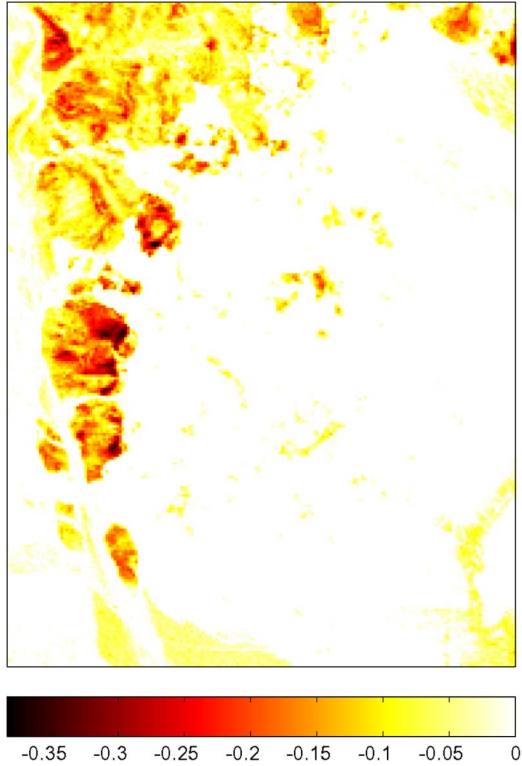
Fig. 9.   Cuprite hyperspectral data ($\cdot$) in the 2-D space defined by the PCA, with endmembers ($\circ$) identifying a triangle enclosing 70% of the data.
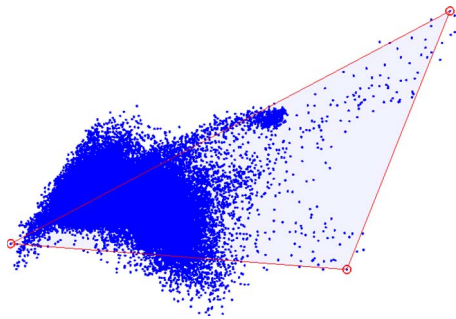
	$\exists\, i\colon \alpha_i < 0$	$\sum_{i=1}^{n} \alpha_i \neq 1$
Unconstrained least-squares (3)	43 065 (90%)	47 746 (99%)
Sum-to-one least-squares (4)	13 997 (29%)	0
Non-negative least-squares [19]	0	47 746 (99%)
Fully constrained least-squares [21]	0	0
Barycentric coordinates [this paper]	14 586 (30%)	0

each data, it is defined between the initial spectrum $\boldsymbol{x}_\ell$ and the one computed with the linear mixture using the estimated abundances $\widehat{\boldsymbol{x}}_\ell$ with

$$\theta(\boldsymbol{x}_\ell, \widehat{\boldsymbol{x}}_\ell) = \cos^{-1}\left(\frac{\langle \boldsymbol{x}_\ell, \widehat{\boldsymbol{x}}_\ell \rangle}{\|\boldsymbol{x}_\ell\|\|\widehat{\boldsymbol{x}}_\ell\|}\right). \tag{14}$$

The spectral angle is invariant with respect to the energy, making it a widely used measure of error for hyperspectral data [39]. The performance of the proposed approach was measured using the spectral angle and compared with the fully constrained least squares. For this purpose, we considered the spectral angle between the initial spectra and, on the one hand, the ones reconstructed using the fully constrained least squares and, on the other, the barycentric coordinates. Fig. 11 shows the histograms of both distributions, demonstrating the small angular error for either techniques, with a mean angle of 0.0866 and 0.0848, respectively. The study of the spectral angle between spectra estimated by each technique showed a very small difference, as shown in Fig. 12.

Fig. 10.   Spatial distribution of the pixels violating the nonnegativity constraint. The value at each pixel corresponds to the smallest α_i when negative and zero otherwise, i.e., when all α_is of the pixel are nonnegative.

with all abundances nonnegative), the violation of the linear model clearly exhibits a spatial structure, which could result from regions with undetected endmembers. These negative abundances were set to zero for the RGB map in the three-channel color Fig. 8. This can be considered as a drawback of using a dimensionality reduction technique, which is PCA in this paper. However, applying the sum-to-one constrained least squares, (4) on the hyperspectral data, without any dimensionality reduction, yielded up to 29% of the data, violating the nonnegativity constraint. Table I presents a quantitative comparison of the constraint violation for different abundance estimation techniques.

In order to measure the performance of the abundance estimation technique, we considered the spectral angle. For

V. CONCLUSION AND ONGOING WORK

In this paper, we presented a new abundance estimation method based on pure geometry, as opposed to conventional matrix inversion techniques. We showed that, once a dimensionality reduction technique such as PCA is applied, it is useless to perform a least-squares estimation. Owing to barycentric coordinates, the abundances are expressed as a ratio of volumes or as a ratio of distances. Since these quantities are often computed for endmember identification, we showed that this method is inherent to well-known endmember extraction techniques, such as N-Findr, SGA, VCA, and ICE. Experimental results showed the relevance of the proposed approach.

The goal of our ongoing work is twofold. On the one hand, we are working on imposing the nonnegativity constraint to barycentric coordinates. This can be applied using simple geometry, as done in this paper. On the other hand, we are interested in a parallel implementation, using graphics hardware (see for instance [40]). It turns out that barycentric coordinates have been largely used in computer graphics applications, such as defining an inclusion test in rasterization or linear interpolation for shading. Therefore, a parallel implementation of the proposed method is natural to graphics hardware.
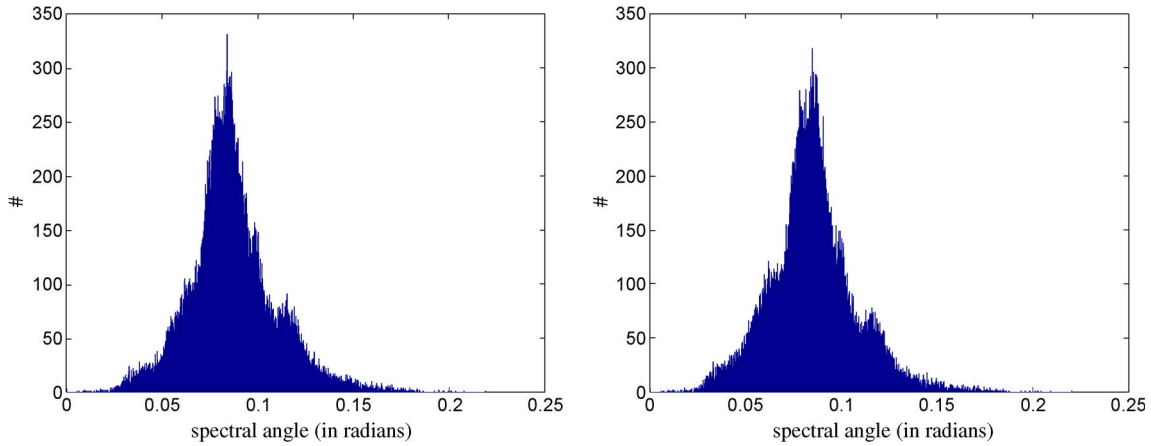
Fig. 11.   Histogram of the spectral angle between the initial spectra and the ones obtained using the abundances estimated with the (left) fully constrained least squares and the (right) proposed technique.
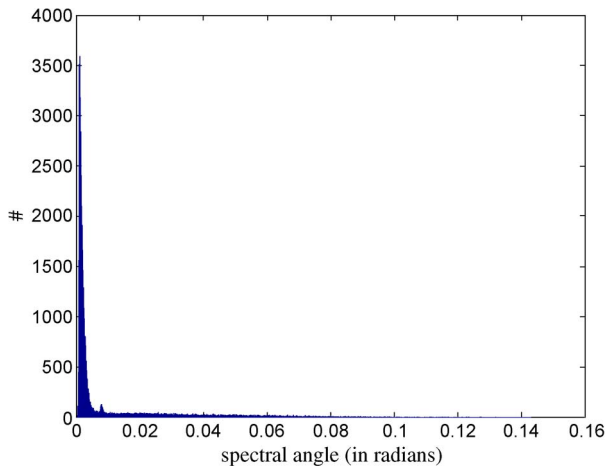

Fig. 12.   Histogram of the spectral angle of the estimated spectra, between the ones obtained from the barycentric coordinates and the fully constrained least-squares techniques.

REFERENCES

[1] S. Moussaoui, H. Hauksdóttir, F. Schmidt, C. Jutten, J. Chanussot, D. Brie, S. Douté, and J. A. Benediktsson, "On the decomposition of mars hyperspectral data by ICA and Bayesian positive source separation," *Neurocomputing*, vol. 71, no. 10–12, pp. 2194–2208, Jun. 2008.

[2] N. Keshava and J. F. Mustard, "Spectral unmixing," *IEEE Signal Process. Mag.*, vol. 19, no. 1, pp. 44–57, Jan. 2002.

[3] K. Guilfoyle, M. Althouse, and C.-I. Chang, "A quantitative and comparative analysis of linear and nonlinear spectral mixture models using radial basis function neural networks," *IEEE Trans. Geosci. Remote Sens.*, vol. 39, no. 10, pp. 2314–2318, Oct. 2001.

[4] U.S. Geological Survey, R. N. Clark, USGS Digital Spectral Library splib06a [Electronic Resource], Sep. 2007.

[5] W. Lawton and E. Sylvestre, "Self-modeling curve resolution," *Technometrics*, vol. 13, no. 3, pp. 617–633, Aug. 1971.

[6] T.-H. Chan, W.-K. Ma, C.-Y. Chi, and Y. Wang, "A convex analysis framework for blind separation of non-negative sources," *IEEE Trans. Signal Process.*, vol. 56, no. 10, pp. 5120–5134, Oct. 2008.

[7] J. M. P. Nascimento and J. M. B. Dias, "Does independent component analysis play a role in unmixing hyperspectral data?" *IEEE Trans. Geosci. Remote Sens.*, vol. 43, no. 1, pp. 175–187, Jan. 2005.

[8] M. Parente and A. Plaza, "Survey of geometric and statistical unmixing algorithms for hyperspectral images," in *Proc. IEEE GRSS WHISPERS*, Reykjavik, Iceland, 2010, pp. 1–4.

[9] M. Winter, "N-FINDR: An algorithm for fast autonomous spectral end-member determination in hyperspectral data: An algorithm for fast autonomous spectral end-member determination in hyperspectral data," in *Proc. SPIE—Imaging Spectrometry V*, 1999, vol. 3753, p. 266.

[10] M. Zortea and A. Plaza, "A quantitative and comparative analysis of different implementations of N-FINDR: A fast endmember extraction algorithm," *IEEE Geosci. Remote Sens. Lett.*, vol. 6, no. 4, pp. 787–791, Oct. 2009.

[11] L. Wang, X. Jia, and Y. Zhang, "Construction of fast and robust N-FINDR algorithm," in *Intelligent Computing in Signal Processing and Pattern Recognition Lecture Notes in Control and Information Sciences*, vol. 345. New York: Springer-Verlag, 2006, pp. 791–796.

[12] C. Chang, C.-C. Wuand, W.-M. Liu, and Y.-C. Quyang, "A new growing method for simplex-based endmember extraction algorithm," *IEEE Trans. Geosci. Remote Sens.*, vol. 44, no. 10, pp. 2804–2819, Oct. 2006.

[13] J. M. P. Nascimento and J. M. B. Dias, "Vertex component analysis: A fast algorithm to unmix hyperspectral data," *IEEE Trans. Geosci. Remote Sens.*, vol. 43, no. 4, pp. 898–910, Apr. 2005.

[14] M. Berman, H. Kiiveri, R. Lagerstrom, A. Ernst, R. Dunne, and J. F. Huntington, "ICE: A statistical approach to identifying endmembers in hyperspectral images," *IEEE Trans. Geosci. Remote Sens.*, vol. 42, no. 10, pp. 2085–2095, Oct. 2004.

[15] A. Zare and P. Gader, "Hyperspectral band selection and endmember detection using sparsity promoting priors," *IEEE Geosci. Remote Sens. Lett.*, vol. 5, no. 2, pp. 256–260, Apr. 2008.

[16] G. Strang, *Introduction to Linear Algebra*, 3rd ed. Cambridge, MA: Wellesley-Cambridge, 2003.

[17] S. Miron, M. Dossot, C. Carteret, S. Margueron, and D. Brie, "Joint processing of the parallel and crossed polarized Raman spectra and uniqueness in blind nonnegative source separation," *Chemometrics Intell. Lab. Syst.*, vol. 105, no. 1, pp. 7–18, Jan. 2011.

[18] S. Jia and Y. Qian, "Constrained nonnegative matrix factorization for hyperspectral unmixing," *IEEE Trans. Geosci. Remote Sens.*, vol. 47, no. 1, pp. 161–173, Jan. 2009.

[19] C. L. Lawson and R. J. Hanson, *Solving Least Squares Problems (Classics in Applied Mathematics)*. Philadelphia, PA: SIAM, 1987.

[20] H. Lantéri, M. Roche, O. Cuevas, and C. Aime, "A general method to devise maximum-likelihood signal restoration multiplicative algorithms with non-negativity constraints," *Signal Process.*, vol. 81, no. 5, pp. 945–974, May 2001.

[21] D Heinz and C. Chang, "Fully constrained least squares linear spectral mixture analysis method for material quantification in hyperspectral imagery," *IEEE Trans. Geosci. Remote Sens.*, vol. 39, no. 3, pp. 529–545, Mar. 2001.

[22] J. S. Cardenas and L. Wang, "Fully constrained linear spectral unmixing: Analytic solution using fuzzy sets," *IEEE Trans. Geosci. Remote Sens.*, vol. 48, no. 11, pp. 3992–4002, Nov. 2010.

[23] S. Robila and L. Maciak, "Considerations on parallelizing nonnegative matrix factorization for hyperspectral data unmixing," *IEEE Geosci. Remote Sens. Lett.*, vol. 6, no. 1, pp. 57–61, Jan. 2009.

[24] F. Schmidt, A. Schmidt, E. Tréguier, M. Guiheneuf, S. Moussaoui, and N. Dobigeon, "Implementation strategies for hyperspectral unmixing using bayesian source separation," *IEEE Trans. Geosci. Remote Sens.*, vol. 48, no. 11, pp. 4003–4013, Nov. 2010.

[25] M. Craig, "Minimum-volume transforms for remotely sensed data," *IEEE Trans. Geosci. Remote Sens.*, vol. 32, no. 3, pp. 542–552, May 1994.

[26] J. Nocedal and S. Wright, *Numerical Optimization*. New York: Springer-Verlag, 1999.

[27] T.-H. Chan, C.-Y. Chi, Y.-M. Huang, and W.-K. Ma, "A convex analysis-based minimum-volume enclosing simplex algorithm for hyperspectral unmixing," *IEEE Trans. Signal Process.*, vol. 57, no. 11, pp. 4418–4432, Nov. 2009.

[28] A. Plaza and C.-I. Chang, "An improved N-FINDR algorithm in implementation," in *Proc. SPIE Algorithms Technol. Multispectral, Hyperspectral, Ultraspectral Imagery XI*, P. E. Shen and S. S. Lewis, Eds., 2005, vol. 5806, pp. 298–306.

[29] L. M. Blumenthal, *Theory and Applications of Distance Geometry*. Oxford, U.K.: Oxford Univ. Press, 1953, (reprinted by Chelsea, Bronx, 1970).

[30] C.-I. Chang, "Orthogonal subspace projection (OSP) revisited: A comprehensive study and analysis," *IEEE Trans. Geosci. Remote Sens.*, vol. 43, no. 3, pp. 502–518, Mar. 2005.

[31] C.-I. Chang, "Further results on relationship between spectral unmixing and subspace projection," *IEEE Trans. Geosci. Remote Sens.*, vol. 36, no. 3, pp. 1030–1032, May 1998.

[32] W. Luo, L. Zhong, B. Zhang, and L.-R. Gao, "Null space spectral projection algorithm for endmember extraction in hyperspectral remote sensing image," (in Chinese), *J. Infrared Millimeter Waves*, vol. 29, no. 4, pp. 307–312, 2010.

[33] W. Luo, L. Zhong, and B. Zhang, "Null subspace analysis for spectral unmixing in hyperspectral remote sensing," in *Proc. Congr. Image Signal Process.*, Washington, DC, 2008, vol. 4, pp. 763–767.

[34] A. Goetz and V. Srivastava, "Mineralogical mapping in the Cuprite mining district, Nevada," in *Proc. Airborne Imaging Spectrometer Data Anal. Workshop*, 1985, pp. 22–31, Jet Propulsion Laboratory Publication 85-41.

[35] G. Swayze, R. Clark, F. Kruse, S. Sutley, and A. Gallagher, "Ground-truthing aviris mineral mapping at Cuprite, Nevada," in *Proc. Summ. 3rd Annu. JPL Airborne Geosci. Workshop, Volume 1: AVIRIS Workshop*, 1992, pp. 47–49, Jet Propulsion Laboratory Publication 92-14.

[36] G. Swayze, "The hydrothermal and structural history of the cuprite mining district, southwestern Nevada: An integrated geological and geophysical approach," Ph.D. dissertation, Univ. Colorado, Boulder, CO, 1997.

[37] L. Miao and H. Qi, "Endmember extraction from highly mixed data using minimum volume constrained nonnegative matrix factorization," *IEEE Trans. Geosci. Remote Sens.*, vol. 45, no. 3, pp. 765–777, Mar. 2007.

[38] O. Duran and M. Petrou, "Spectral unmixing with negative and superunity abundances for subpixel anomaly detection," *IEEE Geosci. Remote Sens. Lett.*, vol. 6, no. 1, pp. 152–156, Jan. 2009.

[39] F. A. Kruse, A. B. Lefkoff, J. W. Boardman, K. B. Heidebrecht, A. T. Shapiro, J. P. Barloon, and A. F. H. Goetz, "The spectral image processing system (SIPS): Interactive visualization and analysis of imaging spectrometer data," *Remote Sens. Environ.*, vol. 2/3, no. 44, pp. 145–163, 1993.

[40] J. Setoain, M. Prieto, C. Tenllado, A. Plaza, and F. Tirado, "Parallel morphological endmember extraction using commodity graphics hardware," *IEEE Geosci. Remote Sens. Lett.*, vol. 4, no. 3, pp. 441–445, Jul. 2007.

Cédric Richard (S'98–M'01–SM'07) was born in Sarrebourg, France, on January 24, 1970. He received the Dipl.-Ing., M.S., and Ph.D. degrees in electrical and computer engineering from the University of Technology of Compiègne, Compiègne, France, in 1994 and 1998, respectively.

He joined the Côte d'Azur Observatory, University of Nice Sophia-Antipolis, France, in 2009, where he is currently a Professor of Electrical Engineering. From 1999 to 2003, he was an Associate Professor with the University of Technology of Troyes (UTT), Troyes, France, where he was also a Professor from 2003 to 2009 and the supervisor of a group of 60 researchers and Ph.D. students. In the winter of 2009 and autumn of 2010, he was a Visiting Researcher at the Department of Electrical Engineering, Federal University of Santa Catarina, Florianópolis, Brazil. He is the author of over 120 papers. His current research interests include statistical signal processing and machine learning.

Prof. Richard was an Associate Editor of the IEEE TRANSACTIONS ON SIGNAL PROCESSING from 2006 to 2010. Since 2005, he has been a member of the board of the federative CNRS research group ISIS on Information, Signal, Images, and Vision. He is also a member of the GRETSI Association Board. He has been an Associate Editor of EURASIP Signal Processing since 2009. In 2009, he was nominated as Liaison Local Officer for EURASIP and member of the Signal Processing Theory and Methods Technical Committee of the IEEE Signal Processing Society. He was a corecipient of the Best Paper Award (with Paul Honeine) for "Solving the pre-image problem in kernel machines: a direct method" at the 2009 IEEE Workshop on Machine Learning for Signal Processing. He has been a Junior Member of the Institut Universitaire de France since October 2010. He was the General Chair of the XXIth francophone conference GRETSI on Signal and Image Processing held in Troyes, in 2007 and of the IEEE Statistical Signal Processing Workshop held in Nice, France, in 2011.

Paul Honeine (M'07) was born in Beirut, Lebanon, on October 2, 1977. He received the Dipl.-Ing. degree in mechanical engineering and the M.Sc. degree in industrial control from the Faculty of Engineering, Lebanese University, Lebanon, in 2002 and 2003, respectively, and the Ph.D. degree in systems optimization and security from the University of Technology of Troyes, Troyes, France, in 2007.

He was a Postdoctoral Research Associate with the Laboratory of Systems Modeling and Dependability from 2007 to 2008. Since September 2008, he has been an Assistant Professor with the University of Technology of Troyes. His research interests include nonstationary signal analysis, nonlinear adaptive filtering, sparse representations, machine learning, hyperspectral data analysis, and wireless sensor networks.

Dr. Honeine is the coauthor (with C. Richard) of the paper that won the 2009 Best Paper Award at the IEEE Workshop on Machine Learning for Signal Processing.